

Magnetic field, differential rotation and activity of the hot-Jupiter hosting star HD 179949

R. Fares^{1,2,3*}, J.-F. Donati², C. Moutou³, M. Jardine¹, A.C. Cameron¹, A.F. Lanza⁴
D. Bohlender⁵, S. Dieters⁶, A.F. Martínez Fiorenzano⁷, A. Maggio⁸, I. Pagano⁴
E.L. Shkolnik⁹

¹ School of Physics and Astronomy, Univ. of St Andrews, St Andrews, Scotland KY16 9SS, UK

² LATT-UMR 5572, CNRS & Univ. P. Sabatier, 14 Av. E. Belin, F-31400 Toulouse, France

³ LAM-UMR 6110, CNRS & Univ. de Provence, 38 rue Frédéric Joliot-Curie, F-13013 Marseille, France

⁴ INAF-Osservatorio Astrofisico di Catania, via S. Sofia, 78 - 95123 Catania. Italy

⁵ HIA/NRC, 5071 West Saanich Road, Victoria, BC V9E 2E7, Canada

⁶ School of Mathematics and Physics, University of Tasmania, PB 37 GP0 Hobart, Tasmania 7001, Australia

⁷ Fundación Galileo Galilei - INAF, Rambla José Ana Fernández Pérez, 7, 38712 Breña Baja, TF - Spain

⁸ INAF-Osservatorio Astronomico di Palermo, Italy

⁹ Lowell Observatory, 1400 W. Mars Hill Road, Flagstaff, AZ, 86001 USA

ABSTRACT

HD 179949 is an F8V star, orbited by a giant planet at $\sim 8 R_*$ every 3.092514 days. The system was reported to undergo episodes of stellar activity enhancement modulated by the orbital period, interpreted as caused by Star-Planet Interactions (SPIs). One possible cause of SPIs is the large-scale magnetic field of the host star in which the close-in giant planet orbits.

In this paper we present spectropolarimetric observations of HD 179949 during two observing campaigns (2009 September and 2007 June). We detect a weak large-scale magnetic field of a few Gauss at the surface of the star. The field configuration is mainly poloidal at both observing epochs. The star is found to rotate differentially, with a surface rotation shear of $d\Omega = 0.216 \pm 0.061 \text{ rad d}^{-1}$, corresponding to equatorial and polar rotation periods of 7.62 ± 0.07 and $10.3 \pm 0.8 \text{ d}$ respectively. The coronal field estimated by extrapolating the surface maps resembles a dipole tilted at $\sim 70^\circ$. We also find that the chromospheric activity of HD 179949 is mainly modulated by the rotation of the star, with two clear maxima per rotation period as expected from a highly tilted magnetosphere. In September 2009, we find that the activity of HD 179949 shows hints of low amplitude fluctuations with a period close to the beat period of the system.

Key words: stars: magnetic fields – stars: planetary systems – stars: activity – stars: individual: HD 179949 – techniques: spectropolarimetry

1 INTRODUCTION

Hot Jupiters (HJs) are giant planets, orbiting close to their host stars (semi-major axis $< 0.1 \text{ AU}$). They represent about 25% of all discovered extrasolar planets. Interactions between the star and the planet can occur in such systems. Star-planet interactions (SPIs) can be of different types: tidal interactions due to the proximity and masses of the two bodies, and plasma interactions due to the magnetic field, e.g. reconnections between stellar and plane-

tary fields (Rubenstein & Schaefer 2000; Cuntz et al. 2000; Grießmeier et al. 2007). Cuntz et al. (2000) suggested that such interactions may enhance stellar activity, this enhancement being modulated by half of the orbital period in the case of tidal interactions, and by the orbital period in the case of magnetospheric interactions. Recently, Fares et al. (2010) suggested that the enhancement due to magnetospheric SPIs is more likely to be modulated on the beat period (synodic period between the stellar rotation and orbital periods) of the system.

Observational studies of HJ hosting stars reported that not all observed systems show hints of interaction; more-

* E-mail: rim.fares@ast.obs-mip.fr

over, for a single system, activity enhancement may be present at some epochs, yet absent at other epochs; finally, a phase lag between the subplanetary longitude and the peak of the activity enhancement is reported in some systems (Shkolnik et al. 2003, 2005, 2008). Different theoretical studies have tried to explain these phase lags. McIvor et al. (2006) considered the case where the stellar field is a tilted dipole, Preusse et al. (2006) adopted a model based on the propagation of Alfvén waves within the stellar wind flow relative to the planet and Lanza (2008) considered a non-potential magnetic field configuration for the closed corona. Cranmer & Saar (2007) modelled the Ca II H & K light curve of a HJ hosting star for different configurations of the stellar magnetic field (having real solar configurations throughout 11 year cycle), and showed that the presence/absence of activity enhancement depends on the magnetic field geometry. A statistical survey of X-ray emission of stars with HJ suggests that they may be ~ 4 times more active than stars with distant planets (Kashyap et al. 2008), but this result was recently contradicted by Poppenhaeger et al. (2010) who found no significant correlations of X-ray luminosity with the planetary parameters in their sample of stars. Magnetohydrodynamic (MHD) simulations of Cohen et al. (2009) show that SPI may increase the X-ray luminosity.

HD 179949 is one of the most studied stars for SPI. It is an F8 star, orbited by a giant planet with minimum mass $m \sin i = 0.916 \pm 0.076 M_{\text{J}}$, semi-major axis $a = 0.0443 \pm 0.0026$ AU and orbital period $P_{\text{orb}} = 3.092514 \pm 0.000032$ d (Butler et al. 2006). The star is reported to undergo epochs of activity enhancement modulated by the orbital period, with a phase lag of $\sim 65^\circ$ (Shkolnik et al. 2008). We organised a multi-wavelength campaign to observe this star in 2009 September, almost simultaneously in spectroscopy (échelle spectrograph @ du Pont telescope @ Las Campanas, PHOENIX @ Gemini and SARG @ TNG), spectropolarimetry (ESPaDOnS @ CFHT) and X-rays (XMM-Newton). With such campaigns one can characterize the system, from the stellar surface (activity and magnetic field) to the stellar corona (X-rays). Simultaneous campaigns also provide an accurate description of the large-scale magnetic field allowing a quantitative modeling of the star-planet interaction.

In this first paper, we present the results of the spectropolarimetric campaign of 2009 September and of a previous campaign in 2007 June. We describe our data in section 2. The magnetic field reconstruction procedure, the magnetic properties and differential rotation of the star are presented in section 3, followed by coronal field extrapolation and activity analysis in section 4 and 5. We summarize the results and discuss their implications in section 6.

2 SPECTROPOLARIMETRIC OBSERVATIONS

In order to map the surface magnetic field of HD 179949 and its evolution, we collected spectropolarimetric data during two observing campaigns in 2009 September and 2007 June. The data set collected in 2009 September is more extensive and of better quality than that collected in 2007 June - hence we analyze it first in the rest of the study. We used ESPaDOnS, a high-resolution spectropolarimeter installed at the 3.6-m Canada-France-Hawaii Telescope (CFHT) in

Hawaii. ESPaDOnS provides spectra that span the whole optical domain (370 to 1000 nm) with a resolution of about 65000 (when used in spectropolarimetric mode).

The data were reduced using a fully automatic tool, called Libre-ESpRIT, installed at the CFHT for the use of the observers (Donati et al. 1997). From collected calibration exposures and stellar frames, Libre-ESpRIT automatically extracts wavelength calibrated intensity and polarisation spectra with associated error bars at each wavelength pixel. Each spectrum is extracted from four subexposures, taken in different configurations of the polarimeter retarders, in order to perform a full circular polarization analysis (Donati et al. 1997). Although it is possible to extract polarisation spectra from two subexposures, using four permits to eliminate (to first order) all systematic error or spurious polarisation (as well as producing a null-polarisation-test profile, to be discussed below). The spectra are normalised to a unit continuum, their wavelength scale refers to the Heliocentric rest frame. Telluric lines serve as a reference to correct the spectral shifts resulting from instrumental effects (e.g. mechanical flexures, temperature or pressure variations). The radial velocity (RV) precision of the spectra, using this calibration procedure, is about 30 m s^{-1} . The RV measurements (listed in Table 1) are in good agreement with the expectations when using the orbital solution of Butler et al. (2006). Fig. 1 represents the RV variations.

In 2009 September, we collected 19 spectra over 15 nights (two stellar rotations). Our data have good S/N ratio, ranging from 940 to 1910 per 2.6 km s^{-1} velocity bin around 700 nm; they sample well the rotation phases. In 2007 June, we collected 10 spectra, covering about 1.5 rotational cycles. The S/N of the spectra around 700 nm ranges from 950 to 1280. The complete log of the observations is listed in Table 1.

The rotational and orbital phases, denoted E_{Rot} and E_{Orb} , were computed using the two ephemerides:

$$\begin{aligned} T_0 &= \text{HJD } 2,451001.51 + 3.092514 E_{\text{Orb}} \\ T_0 &= \text{HJD } 2,451001.51 + 7.6 E_{\text{Rot}} \end{aligned} \quad (1)$$

The first ephemeris is that of Butler et al. (2006), phase zero corresponding to the inferior conjunction (i.e. the planet being between the star and the observer). For the ephemeris giving the rotation phase, we use a rotation period of 7.6 d, identified as the equatorial rotation period (see section 3).

We apply Least-Squares Deconvolution (LSD) to our spectra in order to improve their S/N ratio (Donati et al. 1997). LSD consists of deconvolving each spectrum by a line mask, computed using a Kurucz model atmosphere with solar abundances, temperature of 6250 K (following Santos et al. 2004) and logarithmic gravity of 4.0 cm s^{-2} . The line mask includes the most moderate to strong lines present in the optical domain (those featuring central depths larger than 40% of the local continuum, before any macroturbulent or rotational broadening, about 4,000 lines throughout the whole spectral range) but excludes the strongest, broadest features, such as Balmer lines, whose Zeeman signature is strongly smeared out compared to those of narrow lines. The contribution of each line to the average line profile is weighted by its depth, so that the strongest lines determine the shape of the LSD profile. The cutoff value of 40% was selected at the start of the series of studies of planet-hosting stars (Donati 2007; Moutou et al. 2007;

Table 1. Journal of September 2009 and June 2007 observations. Columns 1–8 sequentially list the UT date, the heliocentric Julian date (at mid-exposure), the complete exposure time, the peak signal to noise ratio (per 2.6 km s^{-1} velocity bin) of each observation (around 700 nm), the rotational and orbital cycles (using the ephemeris given by Eq. 1), the radial velocity (RV) associated with each exposure, the rms noise level (relative to the unpolarized continuum level I_c and per 1.8 km s^{-1} velocity bin) in the circular polarization profile produced by Least-Squares Deconvolution (LSD) and the false-alarm probability of the detection of the magnetic signature.

Date (UT)	HJD	t_{exp}	S/N	Rot. Cycle	Orb. Cycle	v_{rad}	σ_{LSD}	fap
2009	(2455090+)	(s)		(539+)	(1325+)	(km s^{-1})	($10^{-4} I_c$)	
25 Sep	9.73903	4×1260	1750	0.2407	0.2095	−24.58	0.21	< 10^{-8}
25 Sep	9.80652	4×1190	1620	0.2495	0.2314	−24.57	0.24	< 10^{-8}
27 Sep	11.72735	4×1260	1830	0.5023	0.8525	−24.39	0.20	10^{-06}
27 Sep	11.79302	4×1190	1780	0.5109	0.8737	−24.39	0.21	< 10^{-8}
28 Sep	12.73190	4×1260	1350	0.6345	1.1773	−24.61	0.27	0.08
28 Sep	12.79096	4×1190	1410	0.6422	1.1964	−24.60	0.25	0.008
29 Sep	13.73057	4×1260	1910	0.7659	1.5002	−24.45	0.19	0.0002
29 Sep	13.78955	4×1190	1870	0.7736	1.5193	−24.44	0.20	0.00003
30 Sep	14.73560	4×1260	1810	0.8981	1.8252	−24.39	0.21	0.4
30 Sep	14.79547	4×1190	1790	0.9060	1.8446	−24.39	0.21	0.1
01 Oct	15.73477	4×1260	1630	1.0296	2.1483	−24.62	0.23	0.6
01 Oct	15.79425	4×1190	1410	1.0374	2.1676	−24.62	0.28	0.5
02 Oct	16.74999	4×1260	940	1.1632	2.4766	−24.56	0.42	0.0005
03 Oct	17.71701	2×1260	980	1.2904	2.7893	−24.40	0.32	< 10^{-6}
04 Oct	18.80356	4×1260	1650	1.4334	3.1407	−24.55	0.23	< 10^{-6}
05 Oct	19.79055	4×1190	1540	1.5632	3.4598	−24.50	0.25	0.01
07 Oct	21.75237	4×1260	1330	1.8214	4.0942	−24.51	0.27	0.007
10 Oct	24.73615	4×1260	1650	2.2140	5.0590	−24.49	0.23	< 10^{-8}
10 Oct	24.79574	4×1190	1480	2.2218	5.0783	−24.51	0.26	< 10^{-8}
2007	(2454270+)			(430+)	(1058+)			
23 June	4.96537	4×600	1280	0.7178	0.5095	−24.49	0.30	0.03
23 June	5.08479	4×600	1260	0.7335	0.5481	−24.44	0.31	0.1
26 June	8.07869	4×600	1060	1.1275	1.5162	−24.45	0.38	0.4
27 June	8.87788	4×600	1200	1.2326	1.7746	−24.36	0.33	10^{-4}
28 June	9.87806	4×540	950	1.3642	2.0980	−24.55	0.43	0.9
01 July	13.07675	4×600	1000	1.7851	3.1324	−24.54	0.42	0.2
02 July	14.09877	4×600	990	1.9196	3.4629	−24.50	0.43	0.003
03 July	15.00800	4×600	1050	2.0392	3.7569	−24.38	0.38	0.2
03 July	15.07963	4×600	900	2.0486	3.7800	−24.37	0.47	0.3
04 July	15.97775	4×700	870	2.1668	4.0705	−24.52	0.47	0.5

Fares et al. 2009, 2010) by optimising SNR in the LSD profile as a function of line-depth cutoff threshold, using the method of Shorlin et al. (2002). In addition to the intensity and polarization profiles, LSD produces a null profile (labelled N) used as a polarization check and that should show no signal; this helps to confirm that the detected polarization is real and not due to spurious instrumental or reduction effects (Donati et al. 1997). None of the null profiles show a polarisation signature. The multiplex gain provided by LSD in V and N spectra is of the order of 25 with respect to a single line with average magnetic sensitivity, implying noise levels as low as 20 parts per million (ppm).

3 MAGNETIC FIELD AND DIFFERENTIAL ROTATION

3.1 Magnetic modelling

To reconstruct the magnetic map of the star and estimate the surface differential rotation, we use a tomographic imaging technique, called Zeeman-Doppler Imaging (ZDI). ZDI assumes that profile variations are only due to rotational

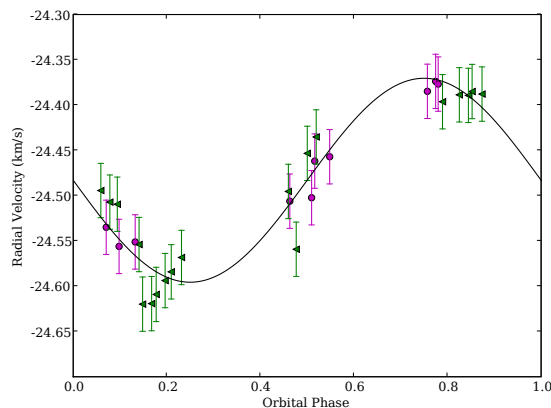


Figure 1. Radial velocities of HD 179949 derived from September 2009 (green triangles) and June 2007 (magenta dots) spectra as a function of orbital phase, with their error bars. The radial velocity curve plotted here is that using the orbital period and amplitude from Butler et al. (2006).

modulation and differential rotation, and can invert (in this context) series of circular polarization Stokes V profiles into the parent magnetic topology and get an estimate of differential rotation at the surface of the star. The magnetic field is described by its radial poloidal, non-radial poloidal and toroidal components, all expressed in terms of spherical-harmonic expansions. The expressions of B_r , B_θ and B_ϕ can be found in Donati et al. 2006; $\alpha_{l,m}$, $\beta_{l,m}$ and $\gamma_{l,m}$ are the spherical harmonics coefficients describing, respectively, the radial poloidal, non-radial poloidal and toroidal components of the magnetic field. This description of the magnetic field has many advantages: both simple and complex magnetic topologies can be reconstructed (Donati 2001); the energy of the axisymmetric and non-axisymmetric modes, as well as of the poloidal and toroidal components is calculated directly from the coefficients of the spherical harmonics. The mean magnetic energy is calculated by the mean over the stellar surface of $B_r^2 + B_\theta^2 + B_\phi^2$. Given the low value of the projected rotational velocity $v \sin i$ ($7.02 \pm 0.50 \text{ km s}^{-1}$ Valenti & Fischer 2005, $6.3 \pm 0.9 \text{ km s}^{-1}$ Groot et al. 1996), the resolution at the surface of the star is limited. We therefore truncate the spherical-harmonic expansions to modes with $\ell \leq 6$. The highest-order spherical harmonics resolvable on a stellar surface typically have orders ℓ , given by $\ell = \max\left(\frac{2\pi v \sin i}{FWHM}, 4\right)$, where FWHM is the full width of half maximum of the intrinsic profile. The highest value of ℓ is closely related to the number of surface resolution elements around the stellar equator, as described in detail by Morin et al. 2010, Sect 3.2. The FWHM of the intrinsic profile of HD 179949 is 8 km s^{-1} (see below), while $v \sin i = 7 \text{ km s}^{-1}$, implying that modes of order $\ell = 5$ or 6 are resolvable.¹ Whereas the longitudinal resolution depends mainly on the $v \sin i$, the latitudinal resolution depends also on the inclination of the star and the phase coverage of the observations.

To compute synthetic circular polarization profiles, ZDI decomposes the surface of the star into 5000 grid cells of similar projected areas (at maximum visibility) and calculates the contribution of each grid cell to the reconstructed profile, given the RV of the cell, the field strength and orientation, the location of the cell and its projected area. Summing the contribution of all grid cells yields the synthetic profile at a given rotation phase. ZDI proceeds by iteratively comparing the synthetic profiles to the observed ones, until they match within the error bars. Since the inversion problem is ill-posed, ZDI uses the principles of Maximum-Entropy image reconstruction (Skilling & Bryan 1984) to retrieve the simplest image compatible with the data. The form we use for the regularisation function is $S = -\sum_{l,m} l(\alpha_{l,m}^2 + \beta_{l,m}^2 + \gamma_{l,m}^2)$. More details about the currently used version of ZDI can be found in Donati (2001); Donati et al. (2006). Other details and assessment of the performance of an earlier version of ZDI code (which was not able to recover simple dipolar magnetic topology) can be found in Brown et al. (1991); Donati & Brown (1997), as well as in appendix B for the currently used version of ZDI.

The models we use to describe the local unpolarized Stokes I and circular polarized Stokes V profiles at each

grid cell are quite simple. Stokes I profiles are modelled by a Gaussian with FWHM of 8 km s^{-1} and central rest wavelength of 550 nm , this Gaussian FWHM fitting best the observations. The linear limb-darkening coefficient is set to 0.6. Stokes V profiles are modelled assuming the weak field approximation, i.e. that the local Stokes V profile is proportional to the effective Landé factor (set to 1.2), the line-of-sight projected component of the magnetic field and the derivative of the local Stokes I profile. This approximation is valid for HD 179949 (whose field strength is a few Gauss). The inclination angle of the star is approximately 60° given the $v \sin i$ of 7 km s^{-1} (Valenti & Fischer 2005), the stellar radius of $1.19 \pm 0.03 R_\odot$ (Fischer & Valenti 2005) and the rotation period of 7.6 d (see section 3.2.1).

Differential rotation (DR) at the surface of the star can be estimated using ZDI. Magnetic regions at different latitudes have different angular velocities, their signatures in the spectra repeat with different recurrence rates. We assume that the rotation at the surface of the star follows $\Omega(\theta) = \Omega_{\text{eq}} - d\Omega \sin^2(\theta)$, where $\Omega(\theta)$ and Ω_{eq} are respectively the angular velocities at a latitude θ and at the equator, and $d\Omega$ is the difference in the rotation rate between the pole and the equator. When the data cover more than a rotational cycle and are well sampled over the rotation cycle, one can in principle measure the recurrence rate of magnetic regions and thus deduce the differential rotation rate of the star. In practice, this is done by reconstructing a magnetic map for each pair of differential rotation parameters (Ω_{eq} , $d\Omega$) at a given information content (constant magnetic energy), and deriving the associated reduced chi-square χ_r^2 at which modelled spectra fit observations. The optimum DR parameters are the ones minimizing χ_r^2 . They are obtained by fitting the surface of the χ_r^2 map with a paraboloid around the minimum value of χ_r^2 (Donati et al. 2003).

3.2 Results

3.2.1 Differential Rotation

To determine the DR of HD 179949, we applied the method described above to 2009 September data (better sampled and covering a longer time span than the 2007 June data set). The χ_r^2 map we obtain forms a well-defined paraboloid shown in Figure 2. The DR parameters we derive are $\Omega_{\text{eq}} = 0.824 \pm 0.007 \text{ rad d}^{-1}$ and $d\Omega = 0.216 \pm 0.061 \text{ rad d}^{-1}$, implying an equatorial rotation period of $7.62 \pm 0.07 \text{ d}$ and a polar rotation period of $10.3 \pm 0.8 \text{ d}$. The equatorial rotation period we find is compatible with the one found by Shkolnik et al. 2003 (≤ 9 days) but slightly higher than the one weakly detected by Wolf & Harmanec 2004 (7.06 days). Collier Cameron (2007) describes $d\Omega$ as a power-law function of the stellar effective temperature; the derived $d\Omega$ for HD 179949 complies with this power law.

For 2007 June data set, we were not able to measure the DR parameters. The data are more noisy than those of 2009 September and the sampling of the rotational cycle is poorer. If we fit the data down to a χ_r^2 value of 0.75 (which we consider normally as overfitting the data), we get the DR parameters similar to those of 2009 September.

¹ We performed a map reconstruction using $\ell_{\text{max}} = 4$, the results are discussed in appendix A.

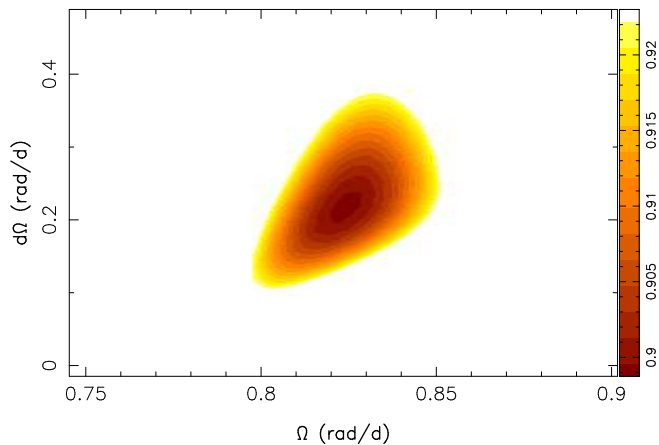


Figure 2. Variations of χ_r^2 as a function of Ω_{eq} and $d\Omega$, derived from the modelling of the Stokes V data set for 2009 September. The outer colour contour corresponds to a 2.7% increase in the χ_r^2 , and traces a 3σ interval (99.7% confidence level) for both parameters taken as a pair.

3.2.2 Magnetic configurations

For 2009 September, the reconstructed Stokes V profiles fit well the data down to a χ_r^2 value of 0.9 (see Fig. 3). The surface magnetic field (Fig. 4), producing these circular polarization profiles, is mainly poloidal (the poloidal energy contributes 90% of the total energy). Low order spherical harmonics contribute the most of the poloidal energy, the dipolar and quadrupolar contribution being about 40% each. 40% of the poloidal field is in axisymmetric modes (note that non-axisymmetric modes correspond to those with $m \geq l/2$ and axisymmetric ones to those with $m < l/2$). The toroidal field constitutes a small fraction of the total field (about 10%).

For June 2007, assuming that the DR did not change over the two epochs, we fit the observed profiles to a χ_r^2 value of 0.9. The field is weaker than September 2009, but is still mainly poloidal (80% of the total energy). The poloidal component is mostly axisymmetric (60%). A summary of the field properties is presented in Table 2. Due to the low S/N values we have for June 2007 data, the reconstructed magnetic energy could be less than the true energy. A Discussion of the effect of S/N and phase sampling on the reconstruction can be found in Donati & Brown (1997) and in appendix B.

Comparing the magnetic field at both epochs, we notice that it is slightly stronger (~ 1 G) in 2009 September than in 2007 June, but this can be due to the better quality of the data set. Cool stars having a Rossby number and a mass greater than 1 and $0.5 M_{\odot}$ respectively seem to have the same trend of magnetic configurations, i.e. mainly axisymmetric poloidal field (Donati & Landstreet 2009, Figure 3). In this context, the large-scale field configuration of HD 179949 is typical for stars with similar masses and rotation rates.

4 LARGE-SCALE CORONAL MAGNETIC FIELD

Using the surface magnetic maps, we can extrapolate the magnetic field to the corona. In this end, we use the Potential Field Source Surface (PFSS) code. This code was first written to model the solar coronal field (van Ballegoijen et al. 1998), and was later developed to be used for stars other than the Sun (Jardine et al. 2002).

We briefly summarise here the PFSS basic principles and underlying assumptions:

- (i) The magnetic field \mathbf{B} is written as the gradient of a scalar potential ψ as $\mathbf{B} = -\nabla\psi$, i.e. the field is potential ($\nabla \times \mathbf{B} = 0$)
- (ii) The three components of the coronal field B_r , B_{θ} and B_{ϕ} are described by a spherical harmonics expansion
- (iii) There is a source surface (of radius R_s) beyond which the field is purely radial $B_{\theta}(R_s) = B_{\phi}(R_s) = 0$
- (iv) The boundary conditions for the radial field at the stellar surface are given by the ZDI magnetic maps (when having these maps, otherwise the magnetic field is modelled by a theoretical model).

Fig. 5 shows as an illustrative example the coronal field lines for the image corresponding to 2009 September, for a source surface located at $3.4 R_{\star}$ (a plausible value given that the mean value of source surface radius of the Sun is $\sim 2.5 R_{\odot}$). Closed loops, connecting regions of different magnetic polarities, reach different heights in the corona ($< R_s$). Open field lines have a configuration close to those of a dipole tilted by $\sim 70^\circ$ relative to the rotational axis. The planet, at $8.1 R_{\star}$, is beyond the source surface. Its magnetic field can reconnect with open field lines, along which the stellar wind can be launched. Given the field geometry and the inclination of the star, the open field lines are almost oriented along the line of sight for some rotational phases (0.2 to 0.35). The large-scale coronal magnetic field in 2007 June is also shown in Figure 5.

The extrapolation of the coronal field is essential to understand the environment in which the HJ evolves. It shows for this star that the large scale magnetic field resembles a tilted dipole.

5 STELLAR ACTIVITY

To study the temporal evolution of chromospheric activity, we analyzed two chromospheric activity proxies : Ca II H & K and H α lines.

For each observing season (2009 September and 2007 June), we calculate a mean profile per proxy. Figure 6 shows these mean profiles for 2009 September. The variability in the proxy is calculated by subtracting the mean profile to the observed ones. The core of the residual profiles vary with time (see Fig. 7). To estimate the residual emission, we fit the line core with a Gaussian (fixing its FWHM and its center at the line center); the equivalent width of the Gaussian gives the residual emission; the residual emission values are mentioned in Table 3. The Ca II H & K and H α residual emission are clearly correlated (Fig. 8, left panel).

The star exhibits variability on both short and long time scales. A modulation of the stellar activity by the orbital period was proposed as a proof of SPI magnetic interactions

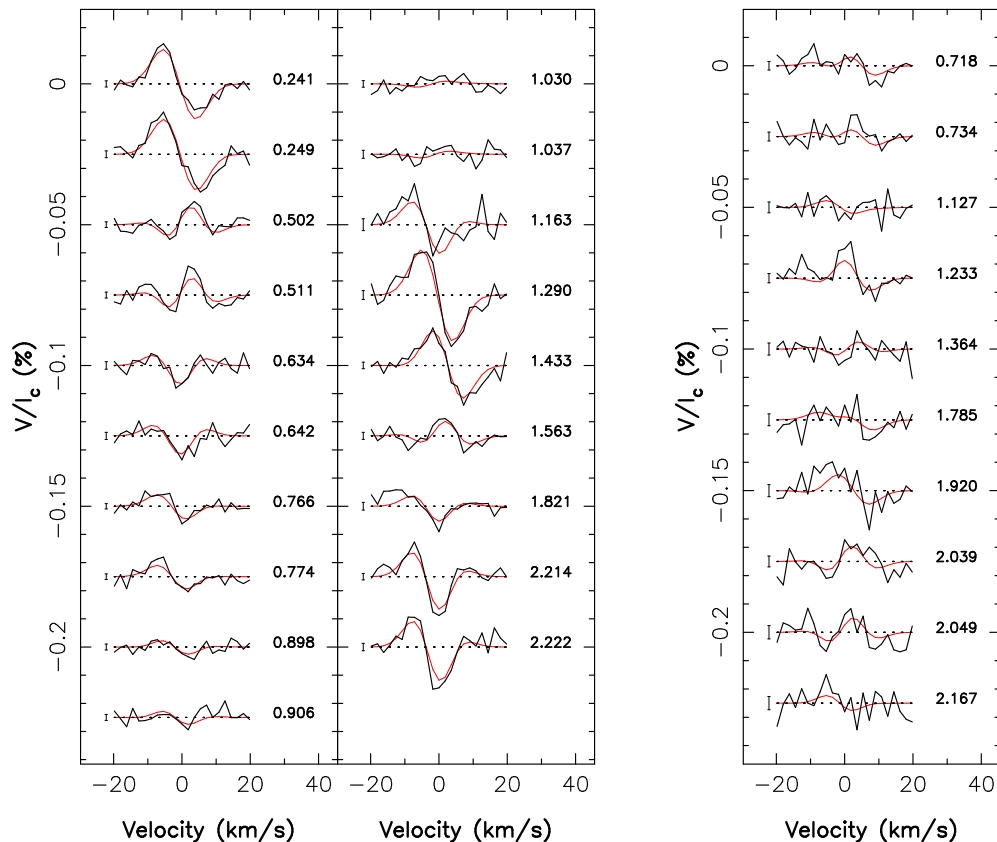


Figure 3. Circular polarization profiles of HD 179949 for 2009 September (left panel) and 2007 June (right panel). The observed and synthetic profiles are shown in black and red respectively. On the left of each profile we show a $\pm 1 \sigma$ error bar, while on the right the rotational cycles are indicated.

Table 2. The field properties for the two epochs of observations. The magnetic field strength averaged over the stellar surface is indicated in the second column (the error bar is of ± 0.3 Gauss for both seasons). The percentage of the poloidal energy relative to the total one and the percentage of the axisymmetric modes (modes with $m < l/2$) energy in the poloidal component relative to the poloidal energy are reported in column 3 and 4 respectively. The energy in the modes having $m = 0$ is reported in column 5.

Epoch	B (G)	E_{poloidal} % of E_{total}	$E_{\text{axisymmetric}, m < l/2}$ % of poloidal	$E_{m=0}$ % of poloidal
September 2009	3.7	90	36	35
June 2007	2.6	80	55	54

(Cuntz et al. 2000). In addition to a modulation with the orbital period, a modulation with the synodic period of the planet with respect to the stellar rotation is in principle possible. The synodic (or beat) period is the period for which the planet faces the same configuration of the magnetic field, and thus if this configuration is favourable for a magnetic interaction (e.g. reconnection), the interaction will happen again after a synodic period. Our aim is thus to search for a periodic modulation of the residual activity. We find that the activity is modulated, to first order, by the stellar rotation, and not by the beat period nor by the orbital period, see figure 9. In order to search for low amplitude periodic fluctuation of the activity, two fitting approaches were used (a linear and a non-linear one). They will be detailed below.

5.1 Linear fit to the data

The open field lines resemble those of a strongly tilted dipole (see section 4), causing the activity to be mainly modulated by half the rotation period. We model the variability by a sum of a linear function (for the long term variability) and two sine waves (one of period P and one of period $P/2$). This model includes the main frequency of the data and its first harmonic (adding a third component at frequency $P/3$ as in Boisse et al. 2011 does not modify the result significantly). Since the star rotates differentially, the rotational period ranges from 7.62 ± 0.07 d to 10.3 ± 0.8 d. For our fit, we fix the period and fit the other parameters of the model using a rejection criterion to omit the points distant by more than 10σ to the model. We explore all the domain of rotational periods, repeating this procedure for every rotational period; the best-fit rotational period is the one minimizing the χ^2_r

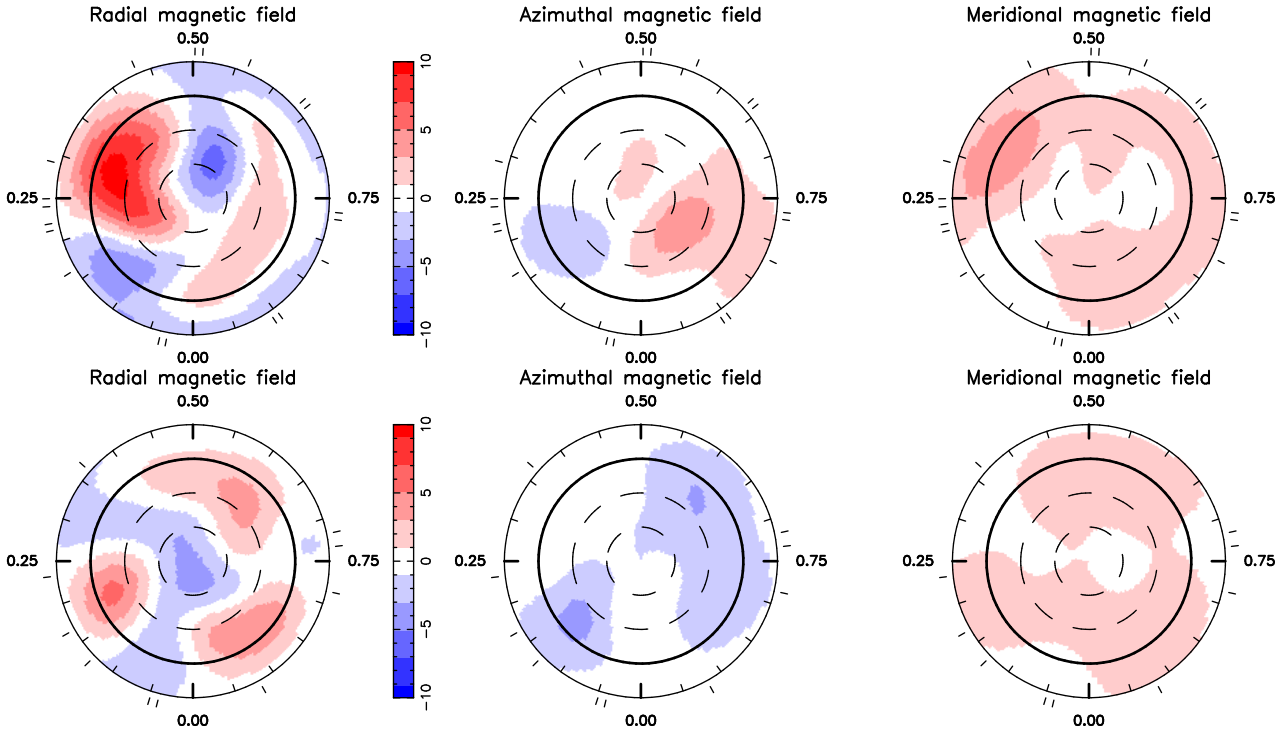


Figure 4. Magnetic maps of HD 179949 for 2009 September (upper panel) and June 2007 (lower panel). The three components of the field in spherical coordinates system in a flattened polar view of the star are presented, down to latitude -30° . The bold circle represents the equator. The small radial ticks around the star represent the rotational phases of our observations. The radial, azimuthal and meridional fields have the same color scale.

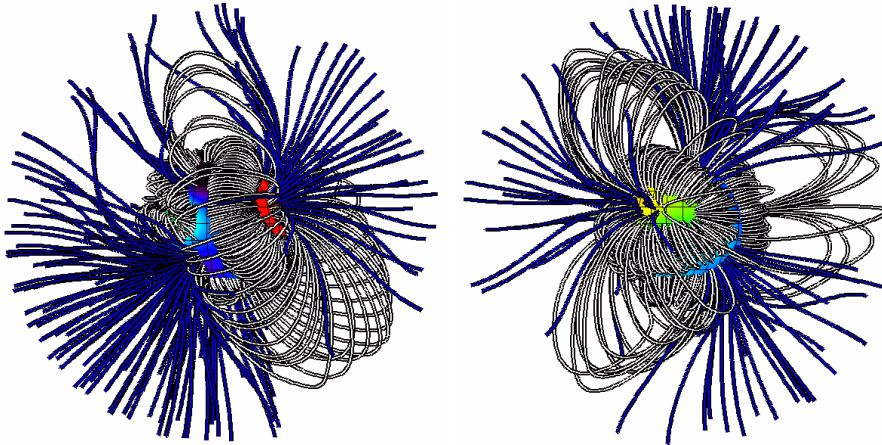


Figure 5. The extrapolated magnetic field of HD 179949 for 2009 September (left panel) and 2007 June (right panel). White lines corresponds to the closed magnetic lines and blue ones to the open field lines (reaching the source surface). The star is shown edged-on.

of the fit (the number of rejected points never exceeds 2 per fit).

Since we are looking for a possible modulation by the beat period and since activity is modulated mainly by rotation, we first subtract the best fit model to the data and look for periodic fluctuations in the residuals (to be called model residuals not to be confused with the residual activity). We fit these model residuals by a sine wave, and calculate the best-fit period of these model residuals.

For 2009 September, the Ca II H & K and H α residual emissions are modulated by $7.75^{+0.55}_{-0.55}$ d and $7.8^{+1.15}_{-1}$ d

respectively, reflecting the fact that both quantities are strongly correlated (see figure 10 and left panel of figure 8, and table 3 for the residual emission values). The slope of the best-fit linear function of H α vs Ca II H & K residual emission is 0.20. To calculate the false-alarm probability (fap) of these signals, we produce 10000 simulated data sets by night-shuffling, and fit each data set using the same procedure as for our observed data set. The number of data sets for which the χ_r^2 of the best-fit period is inferior to the χ_r^2 of our original signal are divided by 10000 to give the fap (Note that we also used the gaussian random noise method

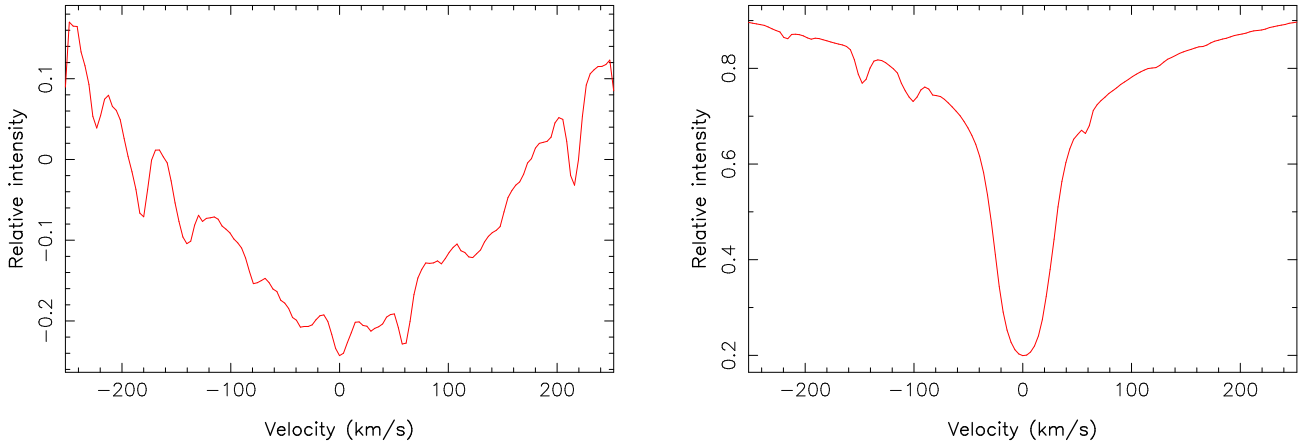


Figure 6. Mean Ca II H & K (left panel) and H α (right panel) profiles for September 2009.

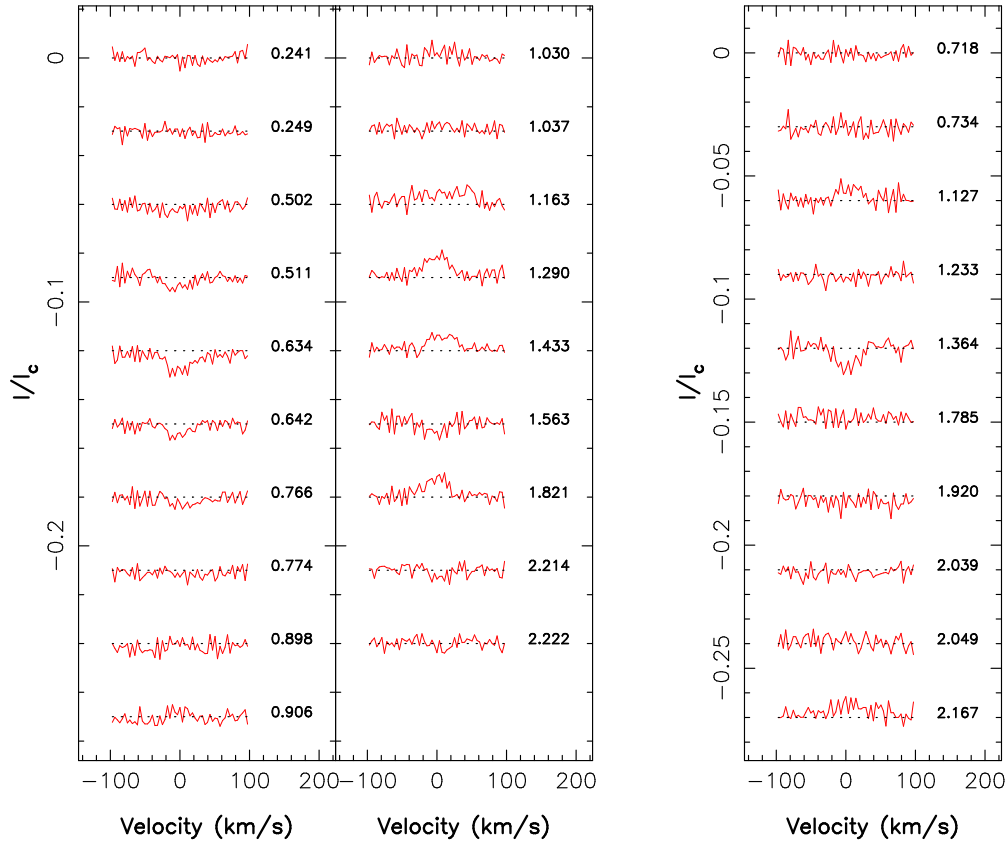


Figure 7. The Ca II H & K residual emission in September 2009 (left panel) and June 2007 (right panel). They show variable features at the center of the line. The rotational phases are indicated on the right of each profile.

to simulate the data sets; the calculated faps are similar to the ones calculated using night-shuffling). The fap of the Ca II H & K periodicity is about 6%, that of H α is higher ($\sim 30\%$).

We then subtracted the best-fit model for each proxy, and calculated the model residuals. The Ca II H & K model residuals are modulated by $5.35^{+0.6}_{-0.65}$ d, the H α ones by $5.5^{+0.7}_{-0.8}$ d, with a fap of 20 and 7% respectively. These model residuals are correlated, as shown in Fig. 8 (right panel). The slope of the H α model residuals vs Ca II H & K model residuals is 0.28, higher than that of the residual emission

(0.20). This correlation may be interpreted as an activity enhancement, seen in both proxies, due to the same physical phenomenon. The beat period of the system ranges from 4.27 to 5.23 days, roughly compatible with the period of the observed fluctuations (within the error bars). The activity enhancement in the model residuals does not correspond to a single orbital phase. This enhancement happens at different orbital cycles (0.86, 2.47 and 4.1), contrary to what was already reported for this system.

For 2007 June, the Ca II H & K residual emission is modulated by $8.6^{+0.65}_{-3.5}$ d (fap of 0.06%). We do not find a

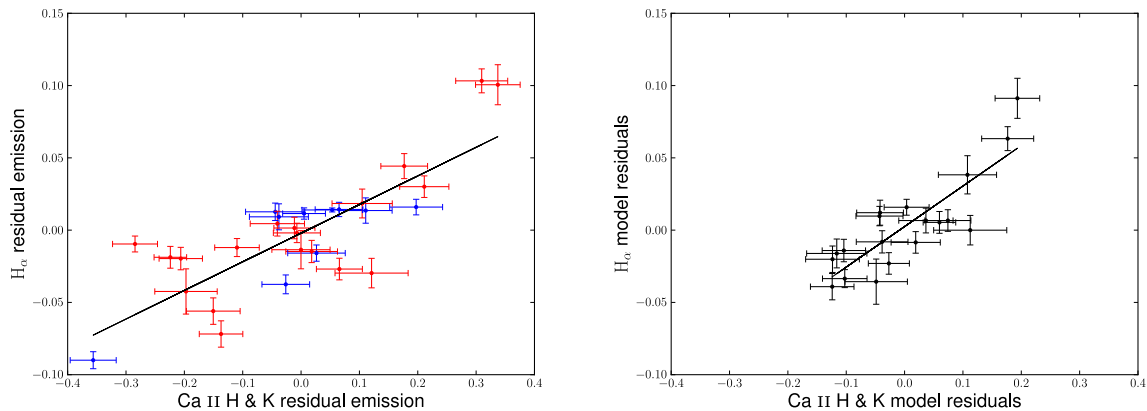


Figure 8. Left panel: $H\alpha$ vs Ca II H & K residual emission for both epochs of observation (2009 September in red and 2007 June in blue). The two quantities are correlated, the Pearson correlation coefficient is 0.8. The line is the best-fit linear function to the data, its slope is 0.20. Right panel: $H\alpha$ and Ca II H & K residuals for 2009 September after subtracting the best-fit model to the data at P_{rot} . The slope of the best-fit linear function is 0.28.

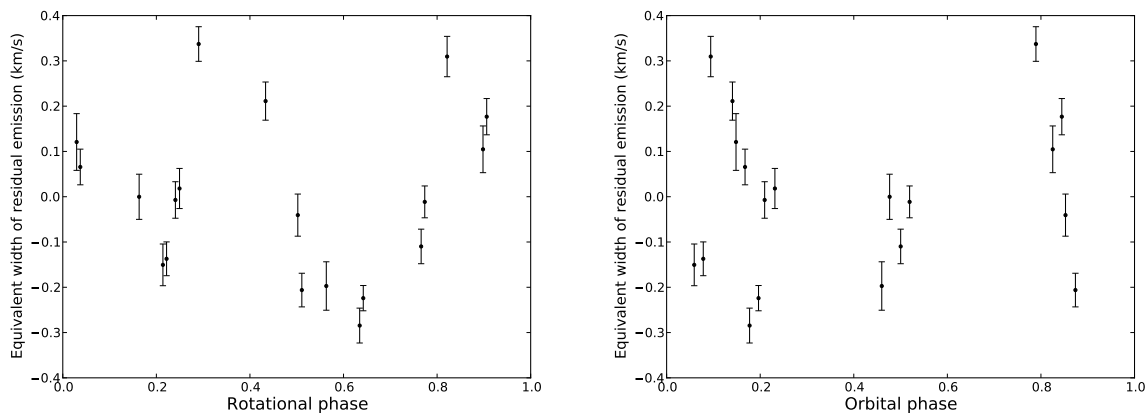


Figure 9. The Ca II H & K residual emission in September 2009 as a function of the rotational phase (left panel) and orbital phase (right panel).

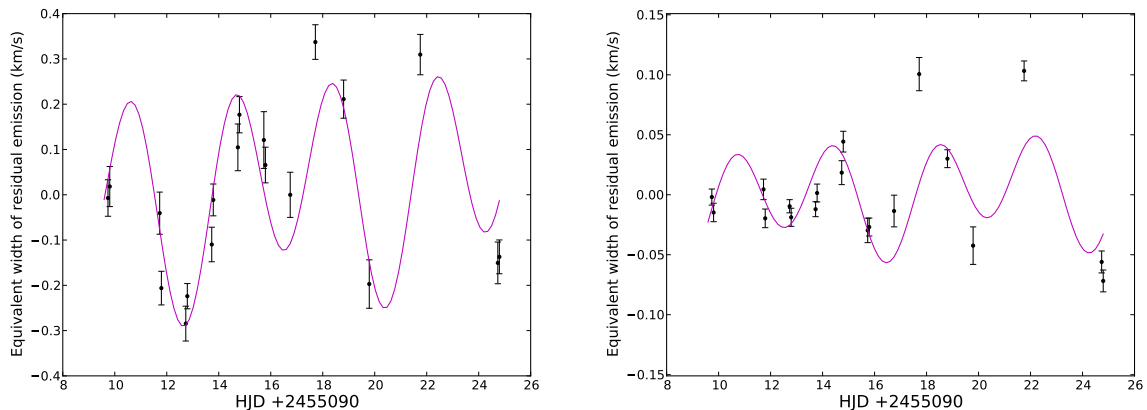


Figure 10. Ca II H & K (left) and $H\alpha$ (right) residual emissions fitted by a linear function and a sum of two sine waves having as periods P and $P/2$ for September 2009. The best fit period to the data is 7.75 d and 7.8 d respectively.

HJD	Ca II H & K residual emission	H α residual emission
	(km s ⁻¹)	(km s ⁻¹)
<hr/>		
2455090+		
9.73903	-0.007 ± 0.040	-0.002 ± 0.007
9.80652	0.018 ± 0.044	-0.015 ± 0.008
11.72735	-0.041 ± 0.047	0.004 ± 0.009
11.79302	-0.206 ± 0.037	-0.020 ± 0.008
12.73190	-0.285 ± 0.039	-0.010 ± 0.005
12.79096	-0.224 ± 0.028	-0.019 ± 0.008
13.73057	-0.110 ± 0.038	-0.012 ± 0.006
13.78955	-0.011 ± 0.035	0.001 ± 0.007
14.73560	0.105 ± 0.052	0.018 ± 0.010
14.79547	0.177 ± 0.040	0.044 ± 0.009
15.73477	0.121 ± 0.063	-0.030 ± 0.010
15.79425	0.066 ± 0.039	-0.027 ± 0.007
16.74999	0.000 ± 0.050	-0.014 ± 0.013
17.71701	0.337 ± 0.038	0.101 ± 0.014
18.80356	0.211 ± 0.042	0.030 ± 0.007
19.79055	-0.197 ± 0.053	-0.042 ± 0.016
21.75237	0.310 ± 0.045	0.103 ± 0.008
24.73615	-0.150 ± 0.046	-0.056 ± 0.009
24.79574	-0.137 ± 0.037	-0.072 ± 0.009
<hr/>		
2454270+		
4.96537	0.065 ± 0.041	0.014 ± 0.005
5.08479	0.053 ± 0.052	0.014 ± 0.001
8.07869	0.197 ± 0.045	0.016 ± 0.005
8.87788	-0.026 ± 0.041	-0.038 ± 0.007
9.87806	-0.356 ± 0.039	-0.090 ± 0.006
13.07675	-0.038 ± 0.051	0.009 ± 0.009
14.09877	-0.044 ± 0.051	0.013 ± 0.006
15.00800	0.005 ± 0.037	0.011 ± 0.004
15.07963	0.026 ± 0.049	-0.016 ± 0.006
15.97775	0.111 ± 0.045	0.014 ± 0.009

Table 3. Ca II H & K and H α residual emission values for September 2009 (upper part of the table) and June 2007 (lower part of the table).

periodic modulation in the model residuals of the Ca II H & K emission after subtracting the best-fit model. No hints of SPI are found for this epoch.

5.2 Non-linear fit to the data

We then used a second period search method, consisting of a non-linear fit of the data, using our original model : a linear function and three sine waves having as periods P_1 , $P_1/2$ and P_2 . We applied this method for the 2009 September data set. The periods we find for the Ca II H & K residual activity are $P_1 = 8.4$ days and $P_2 = 4.87$ days. These periods are compatible with the ones found using the first method within the error-bars. For the H α residual activity, the periods we found are 6.0 and 1.27 days.

Discrepancy between the results found using the two fitting methods may be due to the limited number of unevenly spaced data points, that was also suggested by the high fap probability we got using the first method. The source function of the H α line is dominated by the effects of photoionization and recombination in solar-like stars and F stars, so it is not mainly coupled to the local electron temperature in the chromosphere but principally to the UV radiation field of the star whose main component comes from

the photosphere. The Ca II H & K lines are a more suitable proxy for the non-radiative heating produced by magnetic fields in the chromosphere of an F-type star. A definite detection/no-detection of low amplitude periodic fluctuation needs a larger data set.

6 SUMMARY

We present in this paper the first study of the large-scale magnetic field of the Hot Jupiter hosting star HD 179949. We reconstructed the large-scale surface magnetic field at two observing epochs in 2009 September and 2007 June using ZDI. The field is mainly poloidal (the poloidal component contributing 80 – 90% of the total energy), with a strength of a few Gauss (up to 10 Gauss in some local regions). The field configurations, properties, and polarity show no main changes when comparing both observing seasons. We detected differential rotation at the surface of the star, the latitudinal shear between the pole and the equator being of $d\Omega = 0.216 \pm 0.061$ rad d⁻¹ and the angular velocity at the equator being of $\Omega_{\text{eq}} = 0.824 \pm 0.007$ rad d⁻¹. The equatorial and polar rotation periods are of 7.62 ± 0.07 d and 10.3 ± 0.8 d respectively. The overall field polarity is similar during both seasons, though we can not exclude an evolution on short timescale (Fares et al. 2009). We will continue monitoring the system, observing it at least once a year to study the evolution of the large-scale magnetic field of the star. A comparison between the evolution of the magnetic field of similar spectral type stars, with and without HJs, is the way to understand whether the presence of HJ influences the magnetic field generation (possibly due to tidal interactions).

This star is reported to show activity enhancement modulated by the orbital period for some observing epochs (Shkolnik et al. (2003, 2005, 2008)). To study possible enhancement due to magnetospheric SPI, we studied the coronal large-scale magnetic field and the stellar activity.

The coronal magnetic field is calculated using extrapolation techniques applied to the surface magnetic maps we derived. The field resembles that of a strongly tilted dipole.

The stellar activity proxies (Ca II H & K and H α) show residual emission modulated by the rotation of the star to the first order. We looked for lower amplitude fluctuations by subtracting the rotational modulation to the residual emission. The new Ca II H & K and H α model residuals are periodic and correlated. The variation of these H α model residuals as a function of those of the Ca II H & K shows a trend different from the variation of the H α residual emission as a function of that of the Ca II H & K (having a higher slope value). The periods that best modulate these model residuals roughly match the beat period of the system, suggesting that a SPI magnetospheric interaction may be at the origin of such an effect. To confirm a SPI activity enhancement (or not), a larger data set is needed.

Further observations of the large scale stellar magnetic field are required to study the magnetic cycle length, and possible influences of the planet on the stellar magnetic cycle. Combining observations at different wavelengths will allow us a detailed study of SPI, since it provides information for the system from the stellar surface to the corona.

ACKNOWLEDGMENTS

This work is based on observations obtained with ESPaDOnS at the Canada-France-Hawaii Telescope (CFHT). CFHT/ESPaDOnS are operated by the National Research Council of Canada, the Institut National des Sciences de l'Univers of the Centre National de la Recherche Scientifique (INSU/CNRS) of France, and the University of Hawaii. We thank the CFHT staff for their help during the observations. We also thank an anonymous referee for their comments on our manuscript.

REFERENCES

- Boisse I., Bouchy F., Hébrard G., Bonfils X., Santos N., Vauclair S., 2011, *A&A*, 528, A4+
- Brown S., Donati J.-F., Rees D., Semel M., 1991, *A&A*, 250, 463
- Butler R. P., Wright J. T., Marcy G. W., Fischer D. A., Vogt S. S., Tinney C. G., Jones H. R. A., Carter B. D., Johnson J. A., McCarthy C., Penny A. J., 2006, *ApJ*, 646, 505
- Cohen O., Drake J. J., Kashyap V. L., Saar S. H., Sokolov I. V., Manchester W. B., Hansen K. C., Gombosi T. I., 2009, *ApJL*, 704, L85
- Collier Cameron A., 2007, *Astronomische Nachrichten*, 328, 1030
- Cranmer S. R., Saar S. H., 2007, *ArXiv Astrophysics e-prints*, p. 0702530
- Cuntz M., Saar S. H., Musielak Z. E., 2000, *ApJ*, 533, L151
- Donati J., 2001, in H. M. J. Boffin, D. Steeghs, & J. Cuypers ed., *Astromotography, Indirect Imaging Methods in Observational Astronomy Vol. 573 of Lecture Notes in Physics*, Berlin Springer Verlag, *Imaging the Magnetic Topologies of Cool Active Stars*. pp 207–+
- Donati J., Landstreet J. D., 2009, *Annual Review of Astronomy and Astrophysics*, 47, 333
- Donati J.-F., 2007, *MNRAS*, p. in prep
- Donati J.-F., Brown S., 1997, *A&A*, 326, 1135
- Donati J.-F., Cameron A., Petit P., 2003, *MNRAS*, 345, 1187
- Donati J.-F., Howarth I., Jardine M., Petit P., Catala C., Landstreet J., Bouret J., Alecian E., Barnes J., Forveille T., Paletou F., Manset N., 2006, *MNRAS*, 370, 629
- Donati J.-F., Semel M., Carter B. D., Rees D. E., Collier Cameron A., 1997, *MNRAS*, 291, 658
- Fares R., Donati J., Moutou C., Bohlender D., Catala C., Deleuil M., Shkolnik E., Cameron A. C., Jardine M. M., Walker G. A. H., 2009, *MNRAS*, 398, 1383
- Fares R., Donati J., Moutou C., Jardine M. M., Griefmeier J., Zarka P., Shkolnik E. L., Bohlender D., Catala C., Cameron A. C., 2010, *MNRAS*, 406, 409
- Fischer D. A., Valenti J., 2005, *ApJ*, 622, 1102
- Griefmeier J.-M., Zarka P., Spreeuw H., 2007, *A&A*, 475, 359
- Groot P. J., Pitters A. J. M., van Paradijs J., 1996, *A&AS*, 118, 545
- Jardine M., Collier Cameron A., Donati J., 2002, *MNRAS*, 333, 339
- Kashyap V. L., Drake J. J., Saar S. H., 2008, *ApJ*, 687, 1339
- Lanza A. F., 2008, *A&A*, 487, 1163
- McIvor T., Jardine M., Holzwarth V., 2006, *MNRAS*, 367, L1
- Morin J., Donati J.-F., Petit P., Delfosse X., Forveille T., Jardine M. M., 2010, *MNRAS*, 407, 2269
- Moutou C., Donati J.-F., Savalle R., Hussain G., Alecian E., Bouchy F., Catala C., Collier Cameron A., Udry S., Vidal-Madjar A., 2007, *A&A*, 473, 651
- Poppenhaeger K., Robrade J., Schmitt J. H. M. M., 2010, *A&A*, 515, A98+
- Preusse S., Kopp A., Büchner J., Motschmann U., 2006, *A&A*, 460, 317
- Rubenstein E. P., Schaefer B. E., 2000, *ApJ*, 529, 1031
- Santos N. C., Israelian G., Mayor M., 2004, *A&A*, 415, 1153
- Shkolnik E., Bohlender D. A., Walker G. A. H., Collier Cameron A., 2008, *ApJ*, 676, 628
- Shkolnik E., Walker G., Bohlender D., 2003, *ApJ*, 597, 1092
- Shkolnik E., Walker G., Bohlender D., Gu P., Kürster M., 2005, *ApJ*, 622, 1075
- Shorlin S. L. S., Wade G. A., Donati J.-F., Landstreet J. D., Petit P., Sigut T. A. A., Strasser S., 2002, *A&A*, 392, 637
- Skilling J., Bryan R. K., 1984, *MNRAS*, 211, 111
- Valenti J. A., Fischer D. A., 2005, *VizieR Online Data Catalog*, 215, 90141
- van Ballegooijen A. A., Nisenson P., Noyes R. W., Löfdahl M. G., Stein R. F., Nordlund Å., Krishnakumar V., 1998, *ApJ*, 509, 435
- Wolf M., Harmanec P., 2004, *Information Bulletin on Variable Stars*, 5575, 1

APPENDIX A: RECONSTRUCTED MAP USING LOWER DEGREES OF SPHERICAL HARMONICS

We have reconstructed the magnetic map of HD 179949 using degrees of spherical harmonics up to an order smaller than the one used in the paper, for the purpose of comparison. Indeed, when using $\ell_{max} = 6$, only a small amount of energy is attributed to orders of $\ell > 4$ (about 7% of the total energy). As shown in the formula used to derive ℓ_{max} , it is always possible to resolve up to at least $\ell = 4$, we therefore tested reconstructing the map with $\ell_{max} = 4$ for both observing epochs.

The reconstructed map is shown in Fig. A1. Table A1 lists the field properties using $\ell_{max} = 4$ and $\ell_{max} = 6$ for comparison.

We used the same method as in 3.2.1 to quantify the DR parameters for 2009 September when using $\ell_{max} = 4$. We find DR parameters of $\Omega_{eq} = 0.831 \pm 0.008 \text{ rad d}^{-1}$ and $d\Omega = 0.222 \pm 0.037 \text{ rad d}^{-1}$, implying an equatorial rotation period of $7.56 \pm 0.07 \text{ d}$ and a polar rotation period of $10.3 \pm 0.8 \text{ d}$, compatible with the ones found using $\ell_{max} = 6$. These results are not surprising, since the reconstruction procedure uses Maximum-Entropy image reconstruction, and thus the simplest image compatible with the data is the one to be reconstructed. In our case, low orders are sufficient to describe the field in a reliable way.

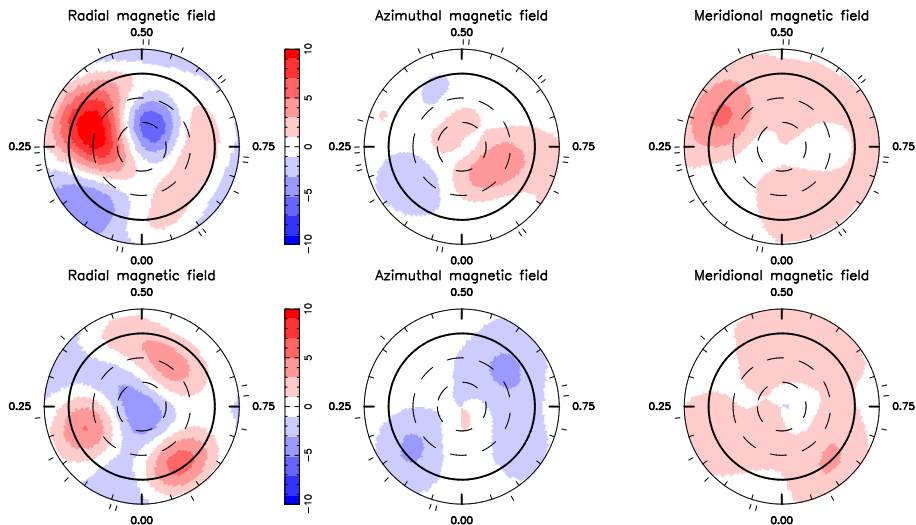


Figure A1. The magnetic map of HD 179949 for 2009 September (upper panel) and 2007 June (lower panel), reconstructed using $\ell_{max} = 4$. The reader can compare to Fig. 4 where the maps were reconstructed using a higher order of spherical harmonics ($\ell_{max} = 6$).

Table A1. The field properties for the two epochs of observations for the reconstructed maps with $\ell_{max} = 4$ and 6. The magnetic field strength averaged over the stellar surface (the error bar is of ± 0.3 Gauss for both seasons) and the percentage of the poloidal energy relative to the total field energy are listed.

Epoch	$\ell_{max} = 6$		$\ell_{max} = 4$	
	B (G)	E_{poloidal} % of E_{total}	B (G)	E_{poloidal} % of E_{total}
September 2009	3.7	90	3.9	90
June 2007	2.6	80	2.9	83

APPENDIX B: EFFECT OF LOW QUALITY DATA ON THE FIELD RECONSTRUCTION

In section 3.2.2, we discuss briefly the effect of low quality data on the map reconstruction. Such effects were discussed elsewhere (Donati & Brown 1997), for an older version of ZDI code. In this appendix, we study the effect of low quality data (low S/N, sparse phase sampling), and show that the new version of the code (based on spherical harmonics decomposition) show similar trends as the old one when dealing with low quality data.

Two major cases will be studied, the first one is the effect of rotational phase gaps in observation on the reliability of the reconstructed map, and the second one is the reliability of a map reconstructed using a low S/N data set.

B1 Rotational phase gaps

To test the effect of rotational phase gaps, we decide to use data from 2009 September data set, selecting spectra with good S/N ratio. We reconstruct two maps out of two sets of data, one with 9 spectra covering rotational phases between 0.2 and 0.8, and one with 7 spectra covering only half of the rotational phases (see Figure B1). Compared to the map reconstructed from 19 spectra (section 3.2.2), both of these maps show a good recovering of the magnetic field of the observed part of the star. Even when half of the rotational cycle is not observed, the reconstructed field on the observed

surface is very similar to the one for the map reconstructed with 19 spectra, but features of the unobserved surface are missed.

B2 Low S/N

One can also question how reliable is a reconstructed map based of spectra with low S/N ratio. In order to test this, we divide the 19 spectra data set of 2009 September to two completely independent subsets, one of 10 spectra with low S/N ratio, and a second one with 9 spectra with the highest S/N ratio of the original dataset. Table B2 lists the properties of the field in each reconstructed map, i.e. magnetic energy and the fraction of the poloidal field. We reconstruct the magnetic maps using both subsets, using $\ell_{max} = 6$ and $\ell_{max} = 4$.

The magnetic energy reconstructed when using a low S/N dataset is, as clear from Table B2, lower than the energy reconstructed when using the whole dataset. However, the reconstructed maps (not shown here) recover most of the reconstructed field of the original map, showing the robustness of the reconstruction. These results are indeed similar to the one found by Donati & Brown (1997).

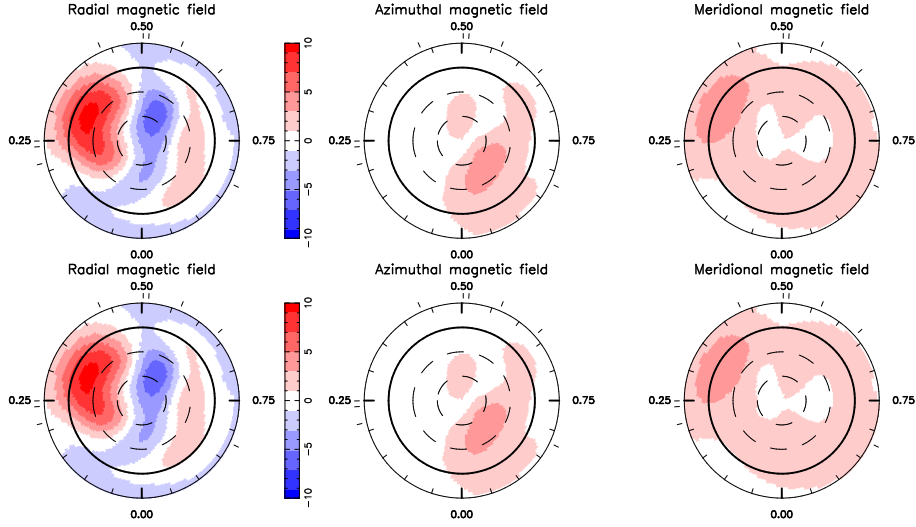


Figure B1. The magnetic map of HD 179949 for 2009 September using 9 spectra with good S/N covering rotational phases from 0.2 to 0.8 (upper panel) and the reconstructed map for 2009 September using only 7 spectra with good S/N covering half of the rotation of the star. The features on the observed surface are well recovered compared to the map in 3.2.2.

Number of spectra	$\ell_{max} = 6$		$\ell_{max} = 4$	
	B (G)	E_{poloidal} % of E_{total}	B (G)	E_{poloidal} % of E_{total}
19 (whole dataset)	3.7	90	3.9	90
9 spectra with high S/N ratio	3.7	90	3.9	90
10 spectra with low S/N ratio	3.2	87	3.3	87

Table B1. The field characteristics when reconstructed using the whole dataset for 2009 September, a subset of only 9 spectra with the higher S/N ratio out of the 19 original spectra, and finally a subset of 10 spectra out of the 19 with the lower S/N ratio. The columns lists the mean magnetic energy and the energy in the poloidal component of the field, for the reconstructed maps using $\ell_{max} = 6$ and $\ell_{max} = 4$ respectively (see text for more details).